Computational Materials Science 85 (2014) 409–419

Contents lists available at ScienceDirect

Computational Materials Science

journal homepage: www.elsevier.com/locate/commatsci

Predicting tensile stretchability of trimmed AA6111-T4 sheets

X.H. Hu [a,*], X. Sun [a], S.F. Golovashchenko [b]

[a] Computational Science and Mathematics Division, Pacific Northwest National Laboratory, Richland, WA 99354, USA
[b] Manufacturing and Processes Department, Ford Research and Advanced Engineering, Scientific Research Laboratory, Dearborn, MI 48124, USA

ARTICLE INFO

Article history:
Received 23 September 2013
Received in revised form 31 December 2013
Accepted 9 January 2014
Available online 15 February 2014

Keywords:
Trimming
Stretchability
Finite element simulations
Aluminum alloys
Edge cracking
Material inhomogeneity

ABSTRACT

An integrated manufacturing process simulation framework has been developed to predict the trimmed edge tensile stretchability of AA6111-T4 sheets by incorporating the burr geometry, damage, and plastic strain from trimming simulations into subsequent tensile stretchability simulations. The influence of the trimming die clearances on the predicted tensile stretching ductility (stretchability) is studied and quantitatively compared with experimental measurements. Stretchability is found to decrease with increasing cutting clearances, and simulation results have successfully captured experimentally observed edge crack initiation and failure mode variations for different trimming clearances. Subsequent computational sensitivity studies reveal that while deburring of previously trimmed edges has little influence on tensile stretchability, removal of trimmed edge initial plastic strain may significantly enhance the subsequent trimmed edge stretchability.

© 2014 Elsevier B.V. All rights reserved.

1. Introduction

Sheet aluminum alloys are increasingly used by the automotive industry in vehicle body panel applications to reduce weight and improve fuel efficiency. In a typical automotive manufacturing environment, shearing processes, such as trimming, piercing, or blanking, are essential operations used to prepare the sheets for subsequent manufacturing processes, including stamping and hemming. However, the shearing processes introduce excessive plastic deformation and damage at the sheared edges and cause burr and sliver formation [1]. The edge damages and geometric features of trimmed edges resulting from improper shearing can compromise the subsequent formability and stretchability due to the formation of premature edge cracks, leading to subsequent split-type failure. The burrs and slivers also negatively influence the surface quality of formed parts.

Although edge cracking of previously sheared parts is a well-known problem for forming, our literature review only uncovers a handful of studies dedicated to this topic regarding aluminum alloys. More studies [2–5] focus on various types of steel sheets with experimental methods that investigate the influence of hole-piercing processes on the subsequent hole extrusion or hole expansion. These studies show that removing burrs [2] from the sheared steel sheets can only slightly improve the hole expansion ratio (HER), a measure of formability for such deformation. Conversely, totally removing the shear affected zone (SAZ), which extends from the sheared edge into the bulk of the sheets, can significantly increase HER [2].

Hubert et al. [6] examined edge cracking during rolling of aluminum sheets previously cut with a continuous disc trimming process, focusing on the influence of rolling contact parameters such as the amount of forward slips on rolling edge cracks' formation. The experiments [6] demonstrate that higher forward slips lead to shallower edge cracks for the same rolling reductions. Their study also shows that employing the annealing process after cutting can significantly reduce the tendency of edge cracking. In the study, no quantitative relationship has been established toward relating the amount of forward slips or cutting parameters to the critical edge crack conditions, e.g., the critical rolling reduction of edge crack formation.

Golovashchenko et al. studied edge cracking during tensile stretching of both aluminum [7] and steel [8,9] blanks previously trimmed along a straight line by shearing tools. In these studies, half dog-bone tensile samples were designed and used to directly measure the edge stretchability while keeping the trimmed edge condition intact. After fracturing of the trimmed part, the experimental observation shows that tensile stretchability is greatly influenced by the cutting clearances during trimming operations, and elongation at fracture decreases up to more than 50% compared to the case with accurate tooling alignment. Two planar failure modes are observed: (1) shear type failure for small clearances and (2) splitting-type failure for large clearances, where the cracking starts from the trimmed edge and propagates normal to the edge across the entire width leading to reduced ductility.

* Corresponding author. Tel.: +1 5093756681; fax: +1 5093724720.
E-mail address: Xiaohua.hu@pnnl.gov (X.H. Hu).

http://dx.doi.org/10.1016/j.commatsci.2014.01.015
0927-0256/© 2014 Elsevier B.V. All rights reserved.

On the computational side, few studies have been performed to predict edge cracking of previously sheared samples due to the challenges in incorporating the various trimmed edge conditions into subsequent forming and deformation simulations. Sartkulvanich et al. [10] use two-dimensional (2D) axisymmetric finite element models to simulate hole blanking and the subsequent hole expansion process of DP590 steel, where burr geometry, as well as strain and damage distributions predicted by the blanking simulations, are carried into the hole expansion process simulations. The predicted HER then was compared to experimental measurements for different blanking clearances. Using the 2D axisymmetric model to simulate the hole blanking process is a reasonable approach. However, the 2D axisymmetric model cannot predict different failure modes (cracking perpendicular or slanted to the edges [11]) during the hole expansion process. Hubert et al. [12] used a 2D plane strain model to simulate the continuous roller trimming process, and the trimmed part's final mesh is extruded into a three-dimensional (3D) model. Edge cracking is studied during rolling, where the cross-sectional mesh of the 3D model correlates to the deformed mesh from the trimming model. The plastic strain and damage incurred during the cutting procedure is mapped into the 3D rolling model, where materials damage is modeled as element removal. The influences of rolling forward slip and cutting clearances were qualitatively studied. The deleted elements on the side surface (LD $\times$ TD) were shown and compared to experimental observations. In the case of small forward slips, the numerical results show almost evenly distributed damaged (or deleted) elements at the burnished and fracture zones of the sheared surface, while the damaged elements are confined to the burnished regions for the larger forward slips. However, for both small and large forward slips, the experimental observations show slanted (about 45°) cracks extending from the burnished to the fracture zones, while the latter indicates much narrower cracks. Due to the limitation of mesh sizes used in the model, the slanted cracking (or shear localization failure) observed experimentally [6] is not captured in the finite element simulations [12].

No numerical studies have been reported for edge cracking during uniaxial tensile stretching tests of previously trimmed samples, although it has been investigated experimentally for aluminum and steel sheets by Golovashchenko [7]. The tensile test is the simplest test to determine material mechanical properties, such as stress–strain relationships, elongation at fracture, and ductility. Accurate tensile test simulations of sheet samples are rather challenging because of two possible deformation instabilities that take place consecutively, i.e., from diffused to localized necking [13]. Deformation instabilities are influenced by many factors, including material constitutive behaviors such as strain hardening model [14], strain rate dependency [15], microstructure inhomogeneity [16,17], and sample geometries (including sample gauge length/width and width/thickness ratios [18,19]). For tensile stretching of trimmed half dog-bone samples, the failure mode and ductility apparently are influenced by the edge deformation and damages induced by the previous cutting processes. Initial edge cracks tend to form, which can propagate along the sample's width [7] and cause premature fracture and reduced ductility. To accurately predict tensile failure behavior of previously trimmed edges, it is necessary to have an adequate material constitutive model; information on the degree of material microstructure-level inhomogeneity, such as the grain and second phase particle distribution; and an appropriate damage model. Most importantly, to accurately predict the stretchability of previously trimmed samples, the model must consider the trimmed edge history, including burr geometry, initial plastic deformation, and damages incurred during the trimming operation. Hence, an integrated manufacturing process simulation framework is needed.

In this paper, we present an integrated computational methodology in predicting tensile stretchability of trimmed edges of AA6111-T4 sheets. The trimming process simulation and associated results are presented elsewhere [20]. A novel computational procedure for carrying over cutting edge information into the subsequent model for the half dog-bone tensile sample is developed. Unlike Hubert et al. [12], where the mesh of 3D rolling model was directly extruded from the deformed mesh of 2D trimming model, the 3D tensile model is generated by the extrusion of the 2D edge geometry obtained from the trimming model using a Python script. To create the geometry of a half dog-bone sample, additional geometric features are added to the model, and the final 3D model then is meshed in Abaqus/CAE. In the tensile model, a vectorized user material subroutine (VUMAT) for Abaqus/Explicit is used for the mapping cutting edge information, such as initial plastic strain and damage from the trimming simulations, into the stretching simulation. In this study, the influence of cutting conditions, specifically the clearance between the shearing edges, on sheared edge stretchability is the primary discussion focus. Simulation results of edge cracking, ductility, and failure modes are examined in comparison with the experimental results. The key factors influencing trimmed edge stretchability, including initial plastic strain and damage, burr material inhomogeneity, and initial material heterogeneity, also are examined and discussed.

2. Integrated modeling methodology

2.1. The trimming model

To accurately predict the edge stretchability of a previously trimmed part, the accurate predictions of the trimmed edge conditions, such as plastic deformation and geometric features, are essential. Hu et al. [20] describe the detailed modeling procedures and material properties used in the trimming models. Fig. 1 illustrates the finite element model setup for the trimming process simulation of a 1-mm-thick (t) AA6111-T4 sheet, where very fine meshes with a mesh size of 6 $\times$ 10 μm^2 is used in the cutting zone to accurately capture the excessive plastic deformation along the trimmed surface and the SAZ. Abaqus/Explicit package is used and the trimming model has 100 elements through the thickness. Four-noded linear plane strain quad elements with reduced integration (CPE4R) and hourglass control are adopted in the model. Adaptive mesh and contact techniques are used to mitigate the problem of excessive distortion in the cutting zone and prevent tool/sheet inner penetration, which may occur due to damage

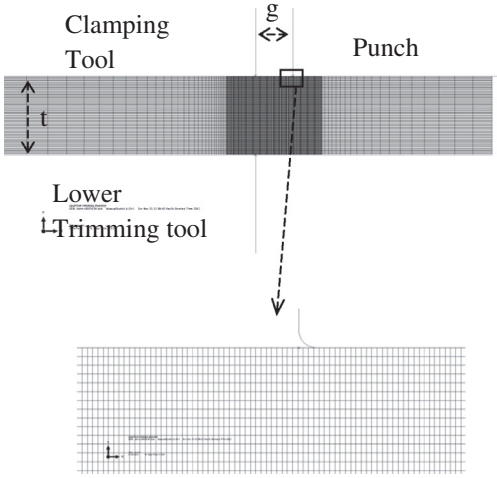

Fig. 1. The finite element trimming model.

and element removal. The AA6111-T4 sheet is assumed to be isotropic elasto-plastic with the work hardening behavior described by a Ludwik power law and material damage represented by a Rice–Tracey ductile fracture model (see material constitutive parameters summarized in Table 1 [20]. The Ludwik parameters are determined by fitting the experimentally measured uniaxial tension flow curves (Fig. 2) up to the true strain (ε) of 0.18 before necking. As can be seen from Table 1, a three-section fitting is used since a one-section fitting cannot satisfactorily represent the experimental curve. It must be noted that the last section ($\varepsilon > 0.145$) also serves as an extrapolation to large strains of the stress–strain curve, where the work hardening index (n) is 0.1809 which is very close to the necking strain of this material during uniaxial tension.

One of the major controlling parameters in trimming is the cutting clearance, which is defined as the ratio of the trimming tool clearance (g) and sheet thickness (t) (see Fig. 1). Similar to experimental observation, the simulation results show that the rollover and burr heights increase with cutting clearance. The predicted burr heights for various cutting clearances are shown to be in quantitative agreements with experimental measurements [20]. Furthermore, the simulation has reproduced both the crack initiation and propagation mechanism, as well as the sliver generation mechanism, as reported in [7] by experimental observations.

2.2. The integration of the trimming results into a 3D tensile stretching model

To preserve all of the predicted trimmed edge through-thickness information, i.e., geometry of the sheared edge, location-dependent damage, and plastic deformations, a full, 3D finite element model is developed to represent the half dog-bone uniaxial tensile sample used by Golovashchenko [7]. The gauge section width of the half dog-bone sample is 12 mm, and, to ensure failure of the tensile sample occurring in the gauge section after final fracture, the transition from the gauge to the grip section is an arc with the radius of 25 mm. Fig. 3 shows the geometry of the half dog-bone sample considered in the current study, where x is the loading direction (LD), y is the transverse section (TD), and z is the normal direction (ND) of the sample.

2.2.1. Burr geometry

The burr geometry of the predicted trimmed edge is obtained by post-processing the trimming simulation results with a Python script to record the nodal coordinates of all the points on the cut edge after full separation of the part and scrap side (Fig. 4(a)). Those coordinates are used to create the 2D outline for this region, representing a cross-section of the 3D tensile model as illustrated in Fig. 4(b). In Fig. 4(b), the free surface of the meshes is extruded into a 3D model (Fig. 4(c)). Finally, the extruded 3D model is modified to have the geometry of the half dog-bone sample with Abaqus/CAE (see Fig. 4(d)). The Abaqus 3D brick element, C3D8R, is used for the model with reduced integration and hourglass control (Fig. 5).

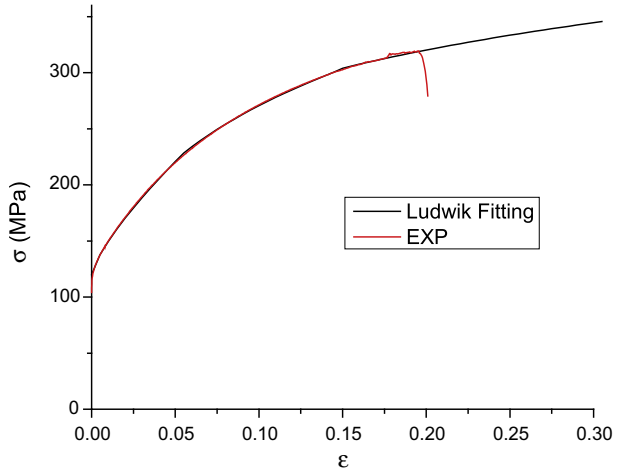

Fig. 2. Ludwik fitting of the uniaxial tensile flow curve of AA6111- T4 Sheet.

Table 1
Ludwik parameters.

$\sigma = \sigma_0^i + k_i\varepsilon^{n_i},\ i = 1-3$			
i (ε)	σ_0	k	n
1 (0, 0.055)	120	981	0.7598
2 (0.055, 0.145)	0	519	0.2828
3 (0.145, –)	0	428	0.1809

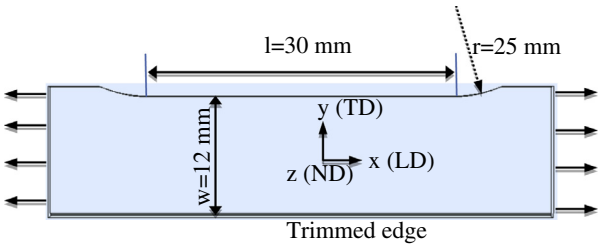

Fig. 3. Top view of the half dog-bone sample geometry used in the 3D finite element model.

2.2.2. Initial plastic strain

In addition to burr geometry, the trimming-model-predicted equivalent plastic strains at the sheared edge and in the SAZ are recorded with a Python script and passed onto the 3D stretching model after mapping. The mapping is accomplished using the vectorized user material subroutine (VUMAT) in Abaqus, where field variables (such as plastic strain) are mapped onto the 3D model based on coordinates [13]. The mapping procedure is similar to that described by Hu et al. [18] where the field variable value of an integration point (i) in the 3D model is chosen to be one (s) stored from the trimming model based on the distance (d_{is}) between the integration point i (X_i, Y_i) in the 3D model and those points stored (x_s, y_s).

$$d_{is} = \left[(X_i - x_s)^2 + (Y_i - y_s)^2\right]^{0.5} \quad (1)$$

The field variable of the sth point of the 2D model which has a minimum distance with the ith point in the 3D model will be assigned to the ith point in the 3D model.

For example, Fig. 6 depicts the interpolation results of the plastic strain from the trimming model to the 3D half dog-bone tensile model. For computational efficiency, the mesh size in the 3D stretching model is considerably larger than that of the 2D trimming model. Hence, the peak values of the smeared field variables in the 3D model are considerably smaller compared to the original 2D trimming model results with a much finer mesh size.

Unlike in multiphase steels, little visible physical damage in the form of void or crack is observed near the fracture surface of many aluminum alloys, including the AA6111-T4 sheet under examination herein [21–23]. Therefore, the trimming-induced edge damage in AA6111-T4 is considered as mostly driven by excessive plastic deformation rather than void coalescence [21–23]. Considering the fact that excessive plastic deformation induced by the trimming process will contribute to the final edge fracture during the

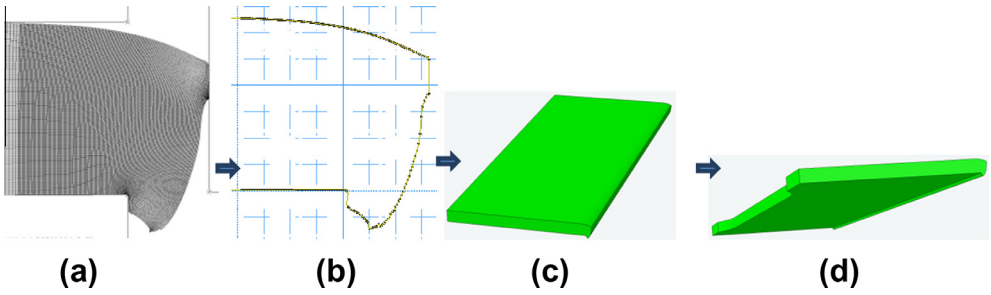

Fig. 4. The procedure to integrate the 2D edge geometry of the trimming model into a 3D half dog-bone tensile sample.

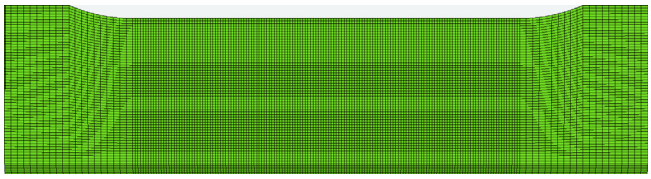

Fig. 5. Mesh generated from the 3D geometry shown in Fig. 3 with the average mesh size within the gauge length measuring 0.2 mm.

subsequent stretching process, its contribution to initial damage (D_0) is calculated by scaling the initial plastic strain of a material point by the maximum limit strain ($\bar{\varepsilon}_f^{\max}$) for uniaxial tension, e.g., 0.6 in the current work. Detailed discussions regarding the damage parameters will be presented in Section 2.3.2.

2.3. Material properties

2.3.1. Work hardening

Consistent with the trimming model, the sheet material is assumed to be isotropic, and the Young's modulus and Poisson's ratio are 70 GPa and 0.33, respectively. An isotropic J2 flow rule is used for the plasticity with the work hardening behavior following a three-section Ludwik power law fitting [20] for the experimental uniaxial tension test data (refer to material parameters tabulated in Table 1).

2.3.2. Material damage model and damage parameters

As with the trimming simulations [20], the material damage is assumed to follow a strain-based accumulated damage fracture criterion:

$$D = \int_0^{\varepsilon_p} \frac{d\varepsilon_p}{\bar{\varepsilon}_f} = 1 \tag{2}$$

where $d\varepsilon_p$ is the plastic strain increment and $\bar{\varepsilon}_f$ is the critical fracture strain, respectively. The accumulated damage model assumes that material failure will occur when the value of damage (D) reaches unity. Because the trimming process is largely a plane strain deformation, the critical fracture strain is assumed be a function of stress triaxiality (η) only [20], which is defined as the ratio between the mean stress (σ_m) and von Mises equivalent stress ($\bar{\sigma}$):

$$\eta = \frac{\sigma_m}{\bar{\sigma}} \tag{3}$$

The Rice–Tracey model [24] has been used for the relations between the critical fracture strain and triaxiality:

$$\bar{\varepsilon}_f = Ae^{-B\eta} \tag{4}$$

Based on the observation of grain shapes near the fracture surface, the Rice–Tracey parameters A and B are 2 and 1.609, respectively, in the trimming model with fine meshes around one-third of the grain sizes (~30 μm) [20]. The determination of these parameters is detailed by Hu et al. [20] and it is based on the measurement of grain aspect ratio near the fracture surface from cross-sectional micrographs of a trimmed sample, which shows excessive deformation at the grain level. The strain calculated at a location in the path of crack propagation is approximately 1.2 with an average triaxility of 0.3 estimated from the finite element calculation. The strain near crack initiation is around 2 with the average triaxiality estimated to be around 0. From these data, the two parameters of the Rice–Tracey model can be obtained. It must be noted that the parameters obtained with this method are approximations, but the values should be much more realistic for the mesh size chosen here than the data used in the literature [1] where much coarser mesh was used, since the AA5xxx and AA6xxx aluminum alloys are found to be very ductile locally [18,25,26].

It should also be noted that the fracture strains varies greatly from different measurement methods [27] and it apparently de-

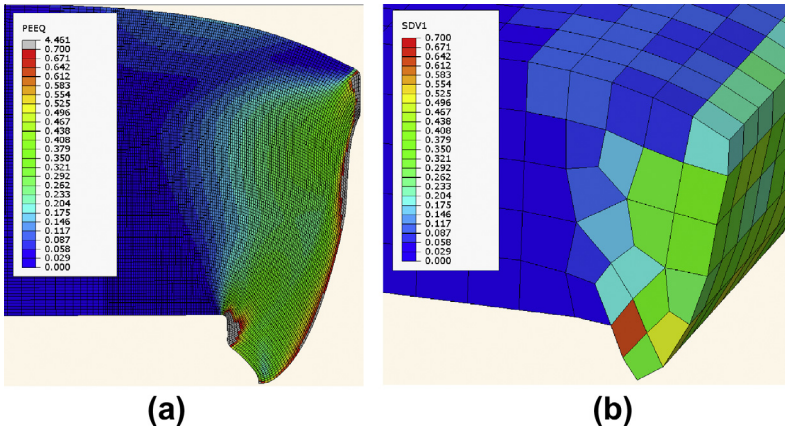

Fig. 6. The mapping results of one of the field variables, i.e., the plastic strain, of the 2D plane strain trimming model (a) to the 3D tensile stretching model (b).

pends on the sample size and measurement resolution along with other factors. The mesh size in the 3D stretching models (~200 μm) is considerably larger than in the 2D model. Thus, it cannot capture the fine deformation concentration and strain gradient near the fracture surface of the sample during the tensile stretching simulations. Therefore, the corresponding fracture strains used in the 3D model should be scaled down accordingly, since the strain of a coarse mesh is actually the average value of strains of many finer meshes representing the same volume of material. Similarly grid-sized-based fracture strain measurements are also reported by experimental measurements [28]. For the AA6111-T4 alloy under examination, the digital image correlation (DIC) technique is used on the surface of electric discharge machining samples (no cutting damage) to assess the maximum strain that can be obtained near fracture. The maximum strain obtained before final fracture is 0.28 (see Fig. 7). Previous experiments at Ford measured with 2-mm-diameter circular grids show the maximum major strain can reach up to 56.2% (0.455 true strains) for the same alloy. The resolution of the DIC measurement depends on the speckle pattern used and effective pixels, stemming from the DIC camera, in pictures used as part of the DIC calculation. The actual strain with a higher resolution (in a smaller area) can be much higher, especially in the region of large strain gradient such as a localized necking band. It has been reported [29] that the strain at the localized shear band in an AA5754 aluminum alloy can be as high as 1.2 using *in situ* scanning electron microscopy (SEM) tensile test pictures for the DIC calculation, while the strain is much lower when using pictures from a charge-coupled device (CCD) camera. DIC strain measurement is also limited by the time resolution of the camera, since deformation is highly localized and develops very fast at the neck location as soon as necking starts, and the last deformation frame before fracture may not have been captured when the time resolution is insufficient. Further complication is that many DIC measurements are from shots from a single camera and the DIC calculation can only assume that the sample is flat on the surface [30]. As for measurements of deformation within the neck after its incipient, 3D DIC techniques are necessary (where two cameras are required for observation at different angles) since there can be extensive through-thickness deformation at the neck. That may explain the results of fracture strains of AA6061-T6 alloys measured by Beese et al. [27]: the average strain is 0.68 measured from cross-sectional area reduction after fracture for tensile testing of several dog-bone shaped samples, much higher than the result from DIC measurement which shows a value of 0.33 for those samples.

In addition to stress triaxiality (η), the fracture strains are also a function of various shear parameters, such as the shear ratio [31], shear factor [32], and lode angle parameters [33]. It needs to be noted that the shear factor and lode angle parameter is related and interchangeable [33]. Because the shear parameters are constant, these factors are not considered in the 2D plane strain trimming model. For considering both triaxiality and shear parameters, some more sophisticated models have been proposed in recent years, especially the Xue–Wierzbicki model [32] and a modified version of it by Bai and Wierzbicki [33], the extended Mohr–Coulomb model [34] and the model proposed by Lou et al. [35]. To determine the parameters of those fracture loci in terms of triaxiality and shear parameter, hybrid inverse methods involving both experimental and numerical studies has been employed. Experiments with many sample geometries are usually required, including dog-bone type samples, planar notched, thickness notched and butterfly samples to cover a wide range of triaxility and shear parameters [27,30,32–36].

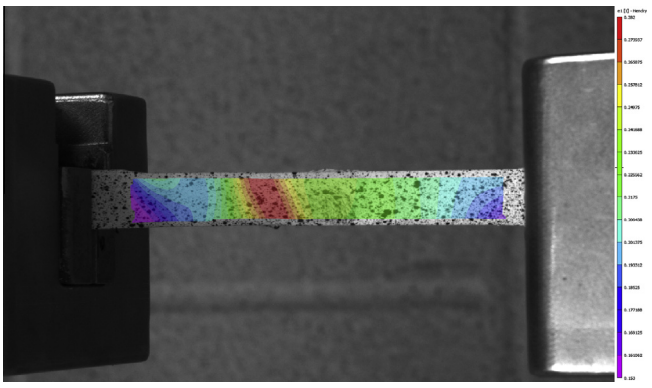

Fig. 7. The major strain contour calculated by DIC at deformation just before fracture.

For uniaxial tension, triaxiality is approximately constant as one-third for the period of uniform deformation and will increase once necking starts. Therefore, the fracture strain ε_f for $\eta = 13$ can be considered as the upper limit strain ($\varepsilon_f^{\max}$) as the fracture strain decreases with triaxiality. The lode angle parameter is 1 at the uniform deformation period and will change once necking starts. The challenge is to obtain the actual fracture strains for different triaxiality and the shear parameters (such as the lode angle parameter) for a specific mesh size used in the finite element stretching simulations. As discussed previously, the fracture strains used for larger mesh should be smaller than those with smaller mesh sizes.

Since the major objective of the current work is to develop an integrated computational framework to consider the effects of trimming in the subsequent stretchability predictions, the relatively simple Rice–Tracey model will be utilized and more sophisticated damage model will be considered in our future studies. A linear down-scaling of the Rice–Tracey parameter A may be the simplest way to reduce the fracture strains for different triaxiality for coarser mesh. However, this type of linear scaling may not be accurate due to the complexity of the deformation gradient variation for complex loading. Furthermore, the deformation modes are also different between trimming (plane strain) and stretching (plane stress). With all the above considerations, an inverse method is adopted in the current studies where a series of parametric studies were performed for the stretchability simulations with different trimming clearances, and the best Rice–Tracey parameters are obtained by comparing the predicted and measured failure modes and total elongation to be: of $A = 0.84$ and $B = 1$. This set of parameters give a fracture strain of 0.6 at $\eta = 13$.

2.4. Material heterogeneity

Polycrystalline materials are inherently heterogeneous due to the plastic anisotropy of a specific crystallite or grain with particular crystalline orientations. The grain level material heterogeneity is represented by the Taylor factor of grains (M_g), and the work hardening behavior of a particular grain is calculated using the ratio R between the Taylor factor of that grain (M_g) and the average Taylor factor ($\bar{M}$) of the model:

$$\sigma_g = R_g \sigma \tag{5}$$

where

$$R_g = \frac{M_g}{\bar{M}} \tag{6}$$

In this work, the Taylor factor is randomly assigned to each integration point of the model (refer to Fig. 8(a)). The initial field variables, i.e., initial plastic strains, are assumed to follow an inverse relationship with R:

$$\varepsilon_g^p(0) = \varepsilon(0)/R \tag{7}$$

as softer grains should experience larger deformation than harder grains. Fig. 8(b) shows the mapped initial plastic strain featuring this scaling with R.

2.5. Obtaining tensile stress versus strain curve

To simulate the half dog-bone tensile test, displacement is applied on both ends of the tensile sample in the x direction in Fig. 2, while those two ends are fixed in the y and z directions.

As described, the Abaqus/Explict finite element package is used for the tensile test simulation of the half dog-bone sample. After the simulation, the true stress–true strain curve is calculated. The calculation is similar to one by Wu et al. [37] and Hu et al. [38], and it is accomplished by averaging the stress and strain tensor at the gauge length in the VUMAT:

$$\bar{\sigma}_{ij} = \frac{1}{N}\sum_{k=1}^{N}\sigma_{ij}, \quad \bar{\varepsilon}_{ij} = \frac{1}{N}\sum_{k=1}^{N}\varepsilon_{ij} \tag{8}$$

where k is the element number and N is the total number of elements.

A more intuitive way of calculating the stresses is summing the reaction forces of all the nodes on the right edge then dividing this by the instant width of the model [39]. The strains can be obtained by taking the logarithm of the ratios between the instant and initial lengths of the model. It has been proven that both methods offer almost identical results for the case of homogeneous mesh in the gauge section. The current method's advantage is that stresses and strains can be calculated quite easily for each increment of the finite element calculation.

Because tensile direction is along the X direction, the $\bar{\sigma}_{11} - \bar{\varepsilon}_{11}$ curve represents the macroscopic tensile stress–strain curve for the model. Fig. 9 is an example of such a curve, and a tensile sample's ductility is represented by the point of strain (E_f) corresponding to the sudden drop of the macroscopic stresses ($\bar{\sigma}_{11}$). The engineering strain (E_e) corresponding to this point is calculated and represents the elongation of the sample:

$$E_e = (\exp(E_f) - 1) \times 100\%. \tag{9}$$

3. Simulations and results

3.1. The tensile failure modes

Tensile stretching simulations are performed for six cutting clearances: 2%, 10%, 21%, 32%, 43%, and 60%, respectively. Fig. 10 illustrates examples of the mapped initial plastic strains for 4 representative cases where Taylor factor scaling is used. These mapped plastic strains contours show that the shear affected zone

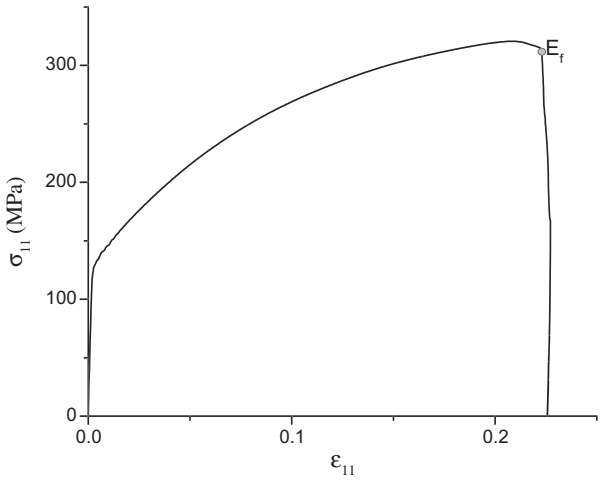

Fig. 9. An example of macrotensile stress–strain curve of a finite element tensile stretching simulation. E_f represents the point of strain corresponding to a sudden drop of stresses.

(SAZ) increase with cutting clearances. It needs to be noted, the meshes generated in Abaqus/CAE are only approximately homogeneous in the SAZ due to complex geometric shapes in the region.

Fig. 11 shows the plastic strain contours of the fractured samples for different clearances calculated by finite element tensile stretch models. Clearly, the calculated stretch failure modes' evolution is in line with experimental observations (Fig. 12 [7]). Samples with small cutting clearances tend to show shear type failure. Meanwhile, as cutting clearances increase, the shear type failure gradually transitions into splitting-type failure for large cutting clearances. Fig. 13 features pictures of final fracture taken during a recent test of smaller gauge length samples. These pictures demonstrate that shear type fractures are present in samples with trimming clearances less than 10%, and splitting-type failures are dominant for clearances larger than 20%. With current simulations, it seems that the predicted failure modes correspond quite well with experimental observations for various trimming clearances.

3.2. Multiple edge cracks

Experimentally, multiple cracks are observed along the edge of a fractured sample after tension of previously trimmed sheets with different clearances. Fine cracks are observed for clearances less than 10% across the trimming fracture zone and bottom edges near the final tensile fracture surface (Fig. 14(a)). Dense, small edge cracks also are observed. Although fine cracks still exists for other

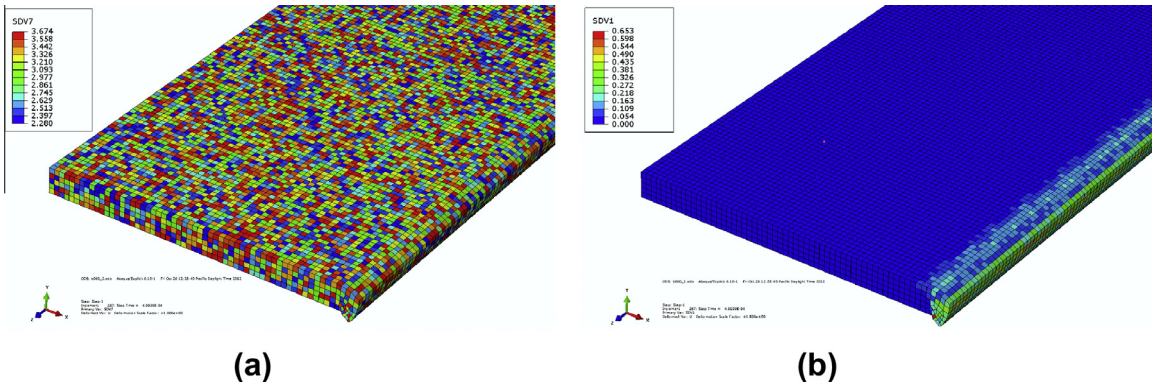

Fig. 8. The mapped Taylor factor (a) and initial plastic strain and (b) contour in the tensile stretching model.

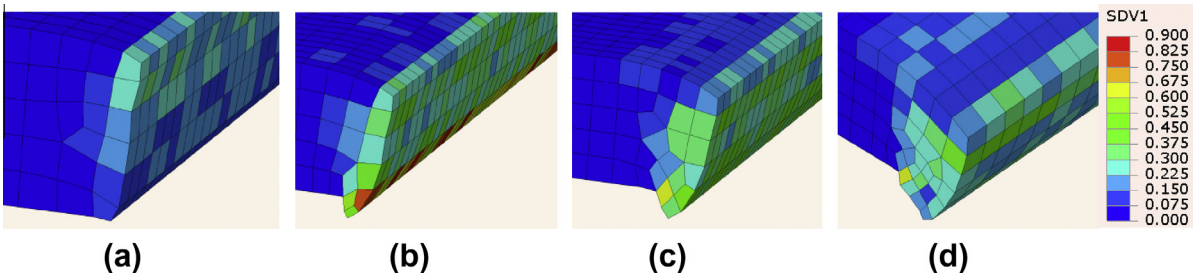

Fig. 10. The initial plastic strain mapped onto the half dog-bone tensile sample for different cutting clearances: (a) 10%, (b) 32%, (c) 43% and (d) 60%.

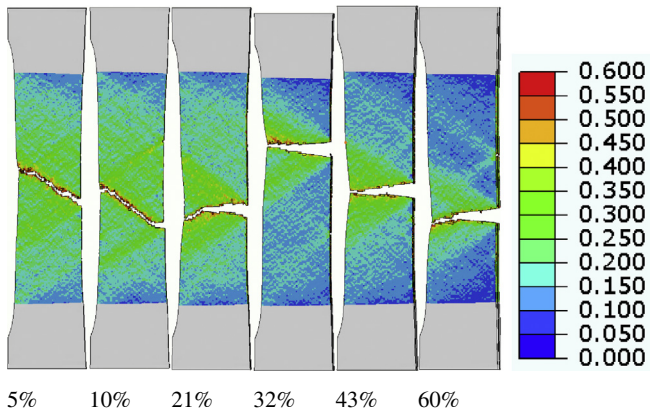

Fig. 11. The equivalent plastic strain contours for fractured samples of different clearances (2–60%) calculated using finite element stretching models with Ludwik power law work hardening and Rice–Tracey fracture ($A = 0.84$, $B = 1$) models.

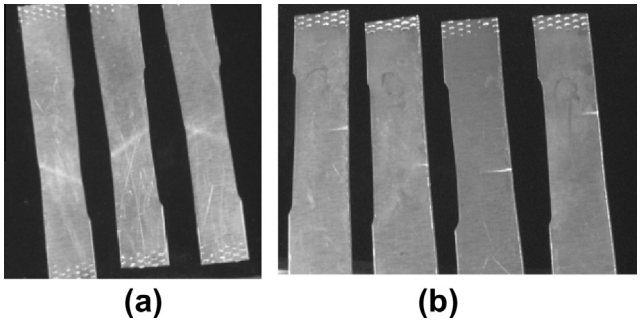

Fig. 12. Images of samples taken before final fracture of the half dog-bone samples tensile stretched after being trimmed with different—(a) small and (b) large cutting clearances.

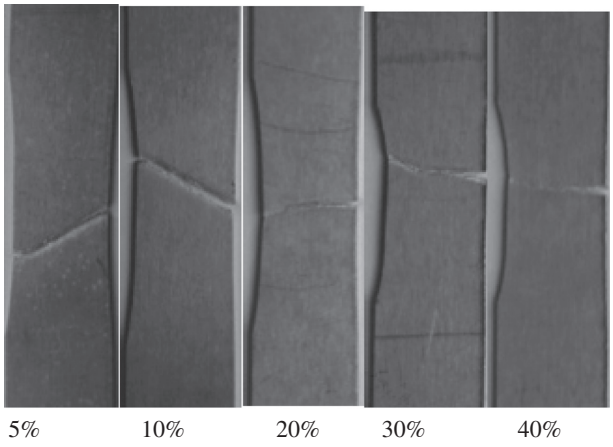

Fig. 13. Pictures of samples after final fracture of smaller gauge length half dong-bone samples with different cutting clearances.

clearances, large, major edge cracks exist at the bottom edge of the burr tips, and the inter-crack distance becomes larger with increasing cutting clearances (Fig. 14(b) and (c)).

Due to the coarse meshes used in the current stretching simulations and use of element removal to represent material damage, the detailed features of fine and edge cracks cannot be captured in the current 3D tensile stretchability simulations because the actual crack opening typically is very small when first initiated and much smaller than the mesh size used here. However, similar observations on multiple edge cracks still can be observed in the finite element simulations represented by element removal (see Fig. 15). Many evenly distributed, edge-damaged spots are visible on the trimmed edge with smaller clearances. With increasing trimming clearance, the hot spots become more discrete, and the predicted inter-crack distance also increases.

3.3. Strain distribution and tensile ductility

Within the tensile gauge length, the predicted results in Fig. 15 indicate that samples with smaller shearing clearances exhibit more evenly distributed plastic strains than those with larger shearing clearances. With more uniform strain distributions, samples with smaller shearing clearance generally indicate the ability to delay damage and localization in the form of shear type failures, leading to higher tensile ductility than those with larger clearances.

In Fig. 15, the calculated stress–strain curves of the models based on Eq. (7) are shown for different cutting clearances, and Fig. 16 demonstrates the obtained elongations in comparison with the experimental results reported by Golovashchenko et al. [7]. From Figs. 16 and 17, it is apparent that the calculated tensile ductility shares the same trend of variation with shearing clearances as with experimental results: the elongation decreases with clearances, and the decrease can be as much as 50%. The predicted elongations (refer to the solid [1]red line with solid diamond symbols in Fig. 16) are slightly higher than the experimental results published by Golovashchenko et al. [7] (the black dashed line with empty upward triangles). However, the detailed trend of variation is close to experimental measurements.

It must be noted that the clearance reported in the literature is the nominal clearance. The actual clearance may change at the end of cutting, and the changes can be sizable if the trimming tool is not stiff enough. Using calibrated clearances for the results of experimental measurements [20], the calculated variation of tensile elongations stemming from finite element simulations is quantitatively close to the experiments (refer to the solid red and black curves in Fig. 16).

4. Factors influencing trimmed edge stretchability

In previous sections herein, we demonstrate an integrated modeling framework for predicting the tensile stretchability of a

[1] For interpretation of color in Figs. 16 and 17, the reader is referred to the web version of this article.

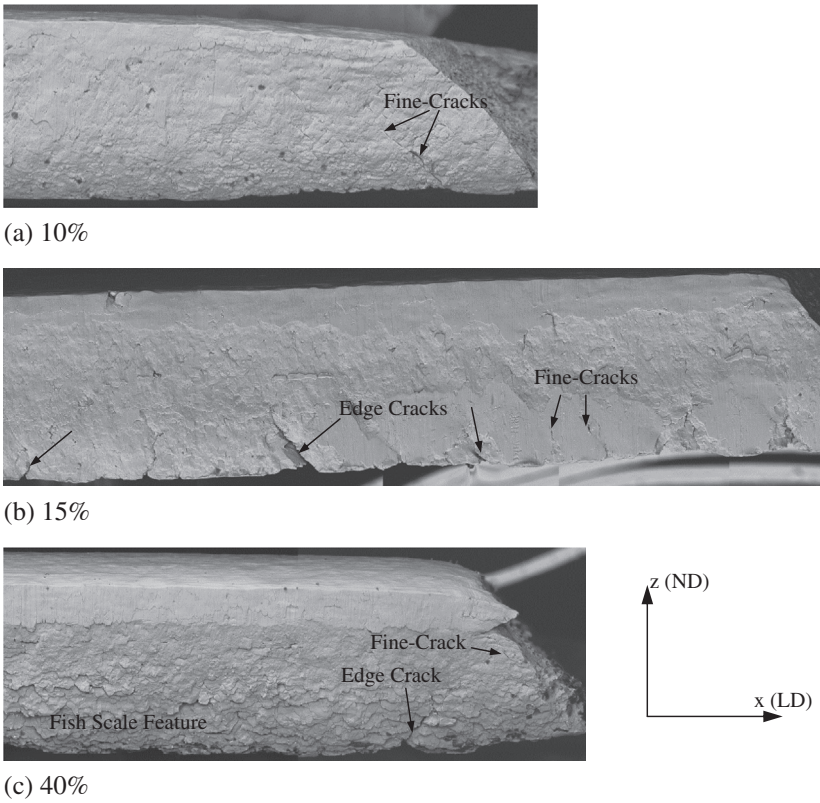

Fig. 14. Through-thickness failure observation with SEM.

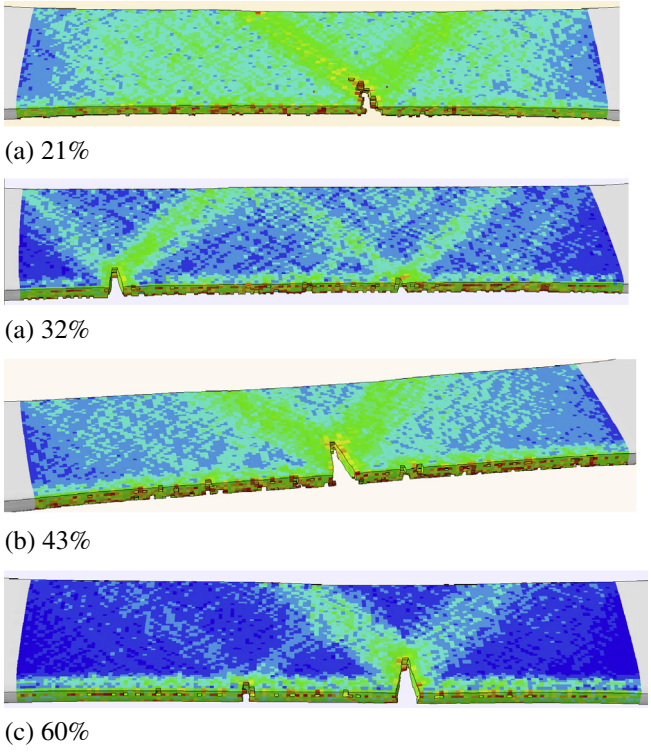

Fig. 15. Multiple necking calculated from finite element simulations and for different cutting clearances.

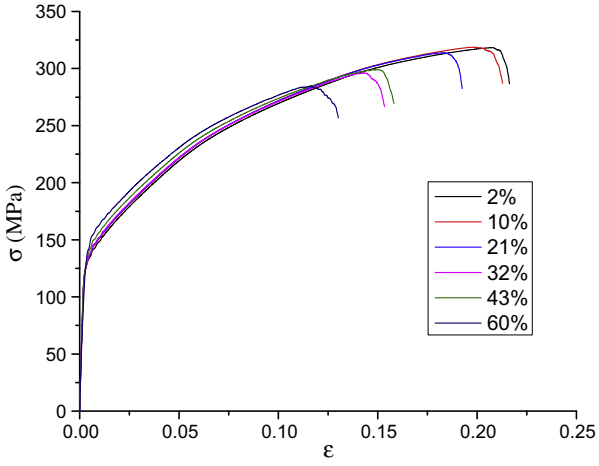

Fig. 16. The calculated tensile true stress–true strain curves for samples with different shearing clearances from 2% to 60%.

trimmed edge by considering its manufacturing history, and the predicted variation of tensile ductility shows good quantitative comparison with experimental measurements with increasing cutting clearances. In general, tensile ductility and failure model can depend on many factors, including materials work hardening behaviors at large strains, damage behavior, burr geometries, and initial damage in terms of initial plastic strain. Material heterogeneity also can play an important role. Specific for the trimmed edges of AA6111-T4 sheets, especially as the work hardening law and damage parameters are considered intrinsic material properties, we numerically examine the influences of other trimming-induced extrinsic factors, i.e., initial trimmed edge geometry, deformation, and damage conditions, on the final stretchability of the trimmed edge. Due to material heterogeneity, the cutting edge information also can vary along the trimmed sample edge, i.e., the tensile direction during the tensile stretching experiments. The

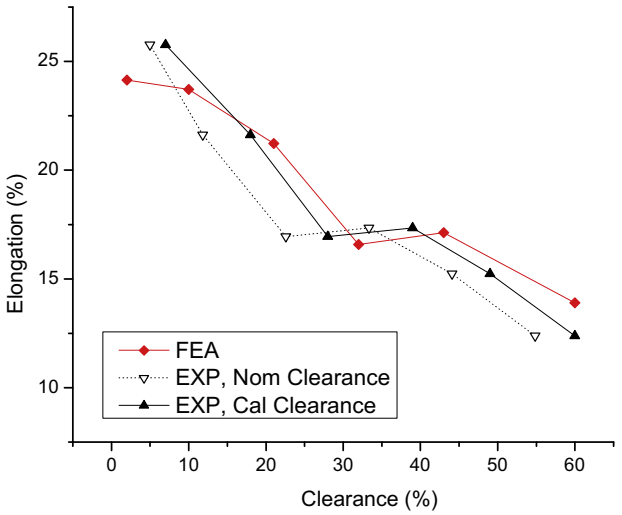

Fig. 17. The calculated elongations for samples of different models in comparison with experimental observations featuring nominal (Nom) or calibrated (Cal) clearances.

goal is to identify key factors influencing trimmed edge stretchability and, if necessary, suggest practical mitigation techniques to enhance it.

4.1. Initial plastic strain

The trimming operation inevitably introduces cutting edge geometric features and large plastic deformations along the trimmed edge. Because the ultimate damage and fracture in aluminum alloys are controlled mostly by excessive plastic deformation, we examine the possibility of improving edge stretchability by removing the trimming-induced initial plastic strains. Similar to the case where edge cracking is reduced by an annealing process before rolling of previously trimmed sheets [12], tensile ductility also may be improved via such as treatment.

In this section, the finite element stretching models use the same trimmed edge burr geometry and material properties as described in Section 3. However, the initial plastic strains and damage predicted by the trimming models are not carried into to the stretching models, and their values are set to zero.

After the initial plastic strain is removed from the stretching models, all samples display that failure modes are mostly shear type for all clearances (Fig. 18(a)), and the elongations for models with large cutting clearances are greatly improved (Fig. 18(b)). Therefore, similar to the rolling results in [12], an effective annealing process may improve formability of previously trimmed aluminum sheets, although such a process also can increase the production costs. Corresponding experimental verification of this observation has been planned for future studies.

4.2. Deburring

Although the process of deburring (burr removal) and/or sliver cleaning can be operationally costly, it has long been an industrial practice after trimming [40] for safety and surface quality considerations, as well as for possible improvement of the subsequent edge stretchability during forming. However, from the work of Adamczyk et al. [2], the formability enhancement from deburring in stretch forming of steel sheets is quite small.

In this section, we examine the effects of burr removal alone and determine its contribution on possible edge stretchability enhancement. The same stretching models for different trimming clearances as those in Section 3 are used with the same set of material properties. Trimming-induced initial plastic strains are maintained in the models, but the burrs are removed (see Fig. 19).

Fig. 20 illustrates the stress–strain curves and elongations obtained after simulations of these models of various clearances. The results indicate that deburring has only a minute influence on tensile stretchability. Ductility actually is slightly reduced for clearances of 2–21% and 43–60%. Meanwhile elongation for clearances of 32% increases, and there is a monotonic change of ductility with trimming clearances. For most clearances, the planar failure modes are nearly the same as those in Fig. 15. From these results, it can be concluded that the deburring process does not improve tensile stretching ductility and failure behavior for AA6111-T4.

4.3. Discussions on material heterogeneity

As previously noted, polycrystalline materials are inherently heterogeneous due to the plastic anisotropy of a particular crystallite or grain with specific crystalline orientations. This kind of heterogeneity is called "grain–grain heterogeneity". The source of microstructure heterogeneity and other heterogeneity, such as surface roughness, dimensional unevenness, and contact conditions,

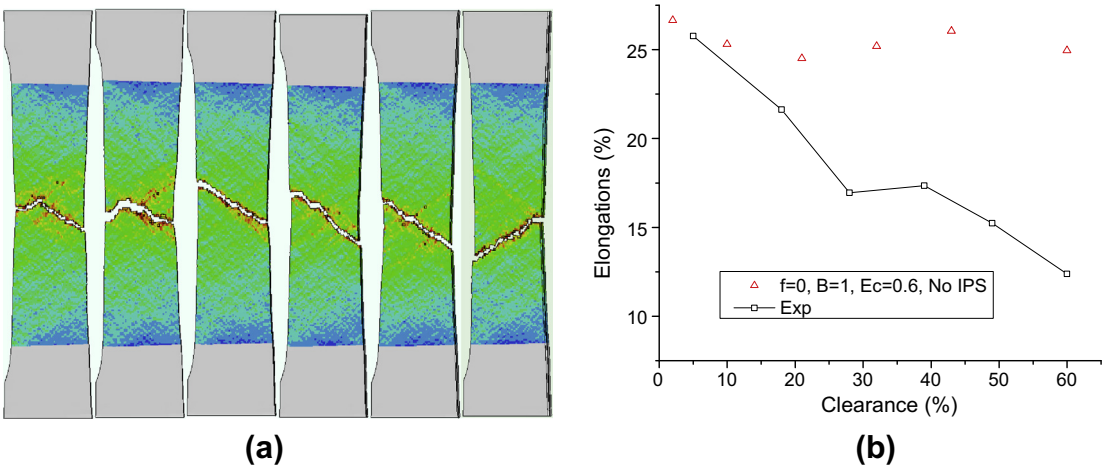

Fig. 18. Results of finite element models of different cutting clearances from 2% to 60%, where the initial plastic strain and damage are set to zero: (a) the equivalent plastic strain contours of the fractured samples and (b) the elongations in comparison with experiments.

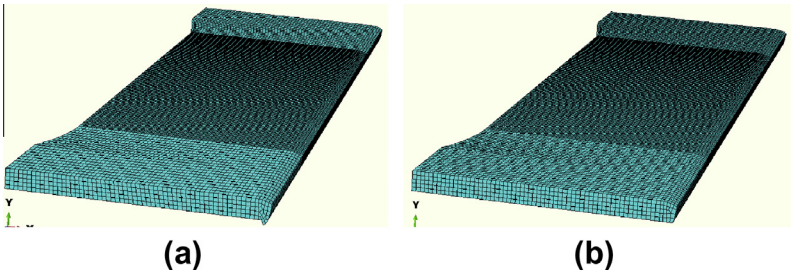

Fig. 19. An example of models for 43% trimming clearance before (a) and after (b) the burr is removed.

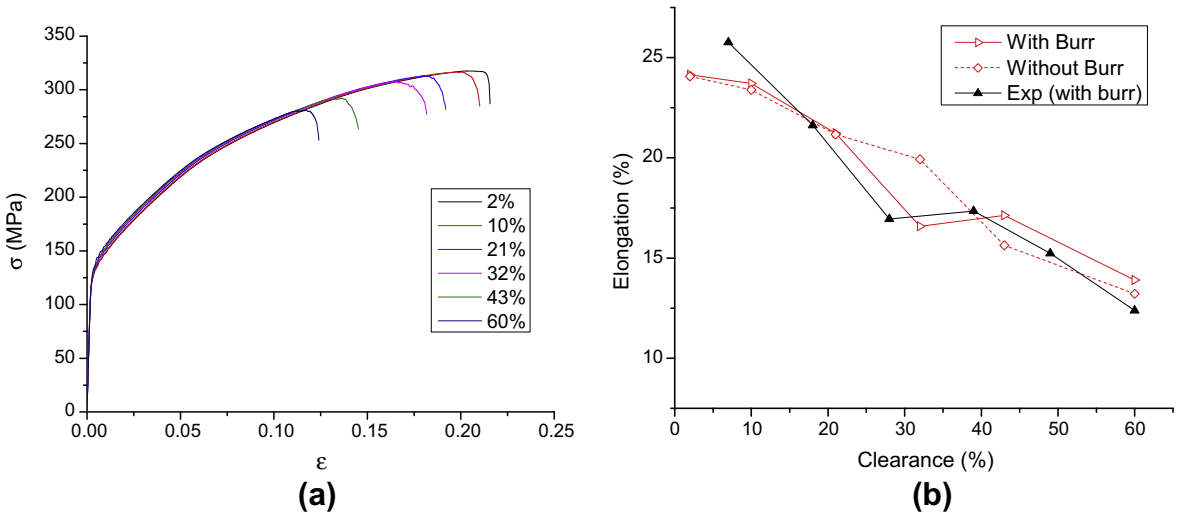

Fig. 20. Simulation results of models with burr removed (deburring): (a) stress–strain curves and (b) elongations.

causes heterogeneous deformation of the sheets during the trimming processes. The subsequent variation of cutting edge geometry can be anticipated. Experimentally, rough cutting edge surfaces have been observed, and large fluctuations of burr height and burr tip geometry have been shown along the cutting edge for large cutting clearances (Fig. 21), especially where roughness and burr height unevenness are very prominent at large cutting clearances (Fig. 21(b)). Detailed SEM after final fractures shows a fish-scale-type fracture surface for cutting clearances of 20% incurred due to trimming.

A full-scale, 3D, microstructure-based finite element model for both the trimming and stretching simulations considering all of these heterogeneities is not feasible due to the excessive computational resources needed. In this current study, the material heterogeneity is considered by randomly assigning Taylor factors to each material point in a model with an average mesh size of 200 μm, where the material properties, initial plastic strains, and/or damages are scaled based on the ratio between the Taylor factor assigned to the point and the average Taylor factor of the model. It must be noted that using the Taylor factor may overstate the grain–grain heterogeneity because the initial average grain size is much smaller than the finite element mesh. By considering other sources of heterogeneities, possibly due to uneven trimming edge geometries, second-phase hard particles ($FeAl_3$), grain size variations, etc., the current work may be thought of as a "combined heterogeneity" factor.

As Hu et al. [18] explain, the planar failure mode depends on the material heterogeneity and the sample width/thickness ratio ($R_{w/t}$) in tensile samples. If the material is perfectly homogeneous, a splitting type of failure is expected even when $R_{w/t}$ is large [18], and predicted fracture starts from the center of the sample, propagating along the width to the edges. In the current study, if the Taylor-factor-based heterogeneity is not considered, the models with trimming clearances below 10% predict similar splitting type failures starting from the center of the samples just as those in [18]. However, for larger clearances, the cracking initiates from the cutting edge and propagates to the other edge.

By considering heterogeneity, the variations of planar failure modes for different clearances are successfully captured. Furthermore, multiple cracking along the cutting edges also is predicted (Fig. 13), which corresponds closely with experimental observations. Due to limited mesh resolution of the tensile stretching finite element model, the shear- or cup-cone-type through-thickness failure modes observed experimentally cannot be captured in the current simulations.

As is discussed previously, the heterogeneity considered here based on Taylor factor variation is taken as a "combined heterogeneity" factor which includes all sources of heterogeneity including

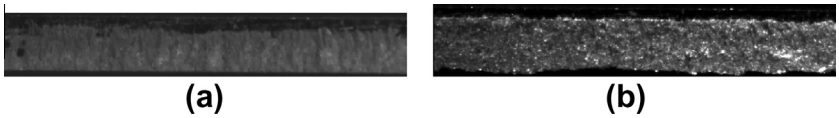

Fig. 21. The edge conditions after trimming for two different clearances: (a) 5% and (b) 30%.

the cutting edge surface roughness and burr-tip variations. Experimentally, there seems to exist a sudden change of edge variation around 10% trimming clearance, below which the trimmed edges are rather smooth, and above which the trimmed edges are very rough (see for example Fig. 21). In the current work, such edge variation dependencies on cutting clearances are not considered since the statistical relationships between the trimming parameter and edge geometrical variations are not yet established. The sudden change of edge variation which is not considered in the simulation work may be the reason of the noticeable difference between the predicted and measured elongations for sample with the nominal trimming clearances less than 10% (Fig. 17).

5. Conclusions

- An integrated computational manufacturing process simulation framework is developed to predict the trimmed edge stretchability under different trimming clearances for AA6111-T4 sheets.
- The framework uses Python scripts to pass the results from the trimming simulations to the subsequent stretching simulations, considering burr geometry, initial plastic strain, and damage at the trimmed edges and in the SAZ. The initial plastic strain distribution is mapped onto the stretching models as field variables through VUMAT in Abaqus/Explicit.
- The predicted tensile stretchability decreases with increasing trimming clearances, and the predictions are shown to be in quantitative agreement with experimental measurements under various trimming conditions.
- Considering initial material inhomogeneity, consistent failure modes also are predicted for the half dog-bone tensile samples under different trimming clearances.
- An annealing process will improve the tensile stretching ductility of trimmed aluminum sheets, while deburring has little influence on ductility or planar failure modes.

Acknowledgements

Pacific Northwest National Laboratory is operated by Battelle Memorial Institute for the US Department of Energy (DOE) under Contract No. DE-AC05-76RL01830. This work was partially funded by the DOE's Office of FreedomCAR and Vehicle Technologies under the Automotive Lightweighting Materials Program managed by Mr. William Joost.

References

[1] S.F. Golovashchenko, Int. J. Mech. Sci. 48 (2006) 1384.
[2] R.D. Adamczyk, G.M. Michal, J. Appl. Metalworking 4 (1986) 157.
[3] R.J. Comstock, D.K. Scherrer, R.D. Adamczyk, J. Mater. Eng. Perform. 15 (2006) 675.
[4] B.S. Levy, C.J. Tyne, J. Mater. Eng. Perform. 17 (2008) 842.
[5] B.S. Levy, M. Gibbs, C.J. Tyne, Metall. Mat. Trans. A 44 (2013) 3635.
[6] C. Hubert, L. Dubar, M. Dubar, A. Dubois, J. Mater. Process. Technol. 210 (2010) 1587.
[7] S.F. Golovashchenko, J. Mater. Eng. Perform. 17 (2008) 316.
[8] S.F. Golovashchenko, A.M. Ilinich, Trimming of advanced high strength steels, in: Presented at 2005 ASME International Mechanical Engineering Congress and RD&D Exhibition, Orlando, FL, USA, 2005.
[9] A.M. Ilinich, S.F. Golovashchenko, L.M. Smith, J. Mater. Process. Technol. 211 (2011) 441.
[10] P. Sartkulvanich, B. Kroenauer, R. Golle, A. Konieczny, T. Altan, CIRP Ann. Manuf. Technol. 59 (2010) 279.
[11] A. Karelova, C. Krempaszky, E. Werner, P. Tsipouridis, T. Hebesberger, A. Pichler, Steel Res. Int. 80 (2009) p 71.
[12] C. Hubert, L. Dubar, M. Dubar, A. Dubois, J. Mater. Process. Technol. 212 (2012) 1049.
[13] X.H. Hu, M. Jain, D.S. Wilkinson, R.K. Mishra, Acta Mater. 56 (2008) 3187.
[14] Z. Marciniak, J. Duncan, S.J. Hu, Mechanics of Sheet Metal Forming, Elsevier, 2002.
[15] J.W. Hutchinson, K.W. Neale, Acta Metall. 25 (1977) 839.
[16] X.H. Hu, D.S. Wilkinson, M. Jain, R.K. Mishra, Int. J. Fract. 164 (2010) 167.
[17] X. Sun, K.S. Choi, W.N. Liu, M.A. Khaleel, Int. J. Plast 2009 (1888) 25.
[18] X.H. Hu, D.S. Wilkinson, M. Jain, P.D. Wu, R.K. Mishra, Mater. Sci. Eng., A 2011 (2002) 528.
[19] V. Tvergaard, Comput. Methods Appl. Mech. Eng. 103 (1993) 273.
[20] X.H. Hu, K.S. Choi, X. Sun, S.F. Golovashchenko, J. Manuf. Sci. Eng.-Trans. Asme (2013), http://dx.doi.org/10.1115/1.4026273.
[21] J. Sarkar, T.R.G. Kutty, K.T. Conlon, D.S. Wilkinson, J.D. Embury, D.J. Lloyd, Mater. Sci. Eng., A 316 (2001) 52.
[22] J. Sarkar, T.R.G. Kutty, D.S. Wilkinson, J.D. Embury, D.J. Lloyd, Mater. Sci. Eng., A 369 (2004) 258.
[23] K. Spencer, S.F. Corbin, D.J. Lloyd, Mater. Sci. Eng., A 325 (2002) 394.
[24] J.R. Rice, D.M. Tracey, J. Mech. Phys. Solids 17 (1969) 201.
[25] A. Ghahremaninezhad, K. Ravi-Chandar, Int. J. Fract. 180 (2013) 23.
[26] D. J. Lloyd, Ductility and bendability in 6000 series automotive alloys, presented at Automotive Alloys, 1999.
[27] A.M. Beese, M. Luo, Y. Li, Y. Bai, T. Wierzbicki, Eng. Fract. Mech. 77 (2010) 1128.
[28] V. Savic, L.G. Hector, J.R. Fekete, Exp. Mech. 50 (2010) 99.
[29] J. Kang, M. Jain, D.S. Wilkinson, J.D. Embury, J. Strain Anal. Eng. Des. 40 (2005) 559.
[30] M. Luo, M. Dunand, D. Mohr, Int. J. Plast. (2012). 32Γ Çô33, 36.
[31] H. Hooputra, H. Gese, H. Dell, H. Werner, Int. J. Crashworthiness 9 (2004) 449.
[32] L. Xue, Damage accumulation and fracture initiation in uncracked ductile solids under triaxial loading—Part I: Pressure sensitivity and Lode dependence, in: Impact and Crashworthiness Lab Report #138, Impact and Crashworthiness Laboratory, Massachusetts Institute of Technology, Cambridge, MA 02139, USA, 2005.
[33] Y. Bai, T. Wierzbicki, Int. J. Plast 24 (2008) 1071.
[34] Y. Bai, T. Wierzbicki, Int. J. Fract. 161 (2010) 1.
[35] Y. Lou, H. Huh, S. Lim, K. Pack, Int. J. Solids Struct. 49 (2012) 3605.
[36] M. Dunand, D. Mohr, J. Mech. Phys. Solids 59 (2011) 1374.
[37] P.D. Wu, S.R. MacEwen, D.J. Lloyd, K.W. Neale, Modell. Simul. Mater. Sci. Eng. 12 (2004) 511.
[38] X.H. Hu, D.S. Wilkinson, M. Jain, R.K. Mishra, J. Eng. Mater. Technol. 130 (2008) 021002.
[39] X.H. Hu, D.S. Wilkinson, M. Jain, R.K. Mishra, Modell. Simul. Mater. Sci. Eng. 15 (2007) 893.
[40] L.K. Gillespie, Deburring and Edgefinishing Handbook, Society of Manufacturing Engineers, Dearborn, MI, 1999.